

# Orbital-Active Dirac Materials from the Symmetry Principle

Shenglong Xu<sup>1</sup> and Congjun Wu<sup>2,3,4,5</sup>

<sup>1</sup>*Department of Physics & Astronomy, Texas A&M University, College Station, Texas 77843, USA*

<sup>2</sup>*Department of Physics, School of Science, Westlake University, Hangzhou 310024, Zhejiang, China*

<sup>3</sup>*Institute for Theoretical Sciences, Westlake University, Hangzhou 310024, Zhejiang, China*

<sup>4</sup>*Key Laboratory for Quantum Materials of Zhejiang Province,*

*School of Science, Westlake University, Hangzhou 310024, Zhejiang, China*

<sup>5</sup>*Institute of Natural Sciences, Westlake Institute for Advanced Study, Hangzhou 310024, Zhejiang, China*

Dirac materials, starting with graphene, have drawn tremendous research interests in the past decade. Instead of focusing on the  $p_z$  orbital as in graphene, we go a step further and study orbital-active Dirac materials, where the orbital degrees of freedom transform as a two-dimensional irreducible representation of the point group. Examples of the orbital-active Dirac materials occur in a broad class of systems including transition metal oxide heterostructures, transition metal dichalcogenide monolayers, germanene, stanene, and optical lattices. We unify different systems based on the symmetry principle. We show that the band structure of the orbital-active Dirac material features Dirac cones at  $K(K')$  and quadratic band touching points at  $\Gamma$ , regardless of the origin of the orbital degrees of freedom. In the strong anisotropy limit, flat bands appear due to the destructive interference of hopping. These new features render the orbital-active Dirac material an even wider playground for searching exotic states of matter, such as Dirac semi-metal, ferromagnetism, Wigner crystallization, quantum spin Hall state and quantum anomalous Hall state.

## I. INTRODUCTION

Graphene has opened up a new era of topological materials, followed by the discovery of topological insulators, topological superconductors, and semi-metals in both two and three dimensions (See reviews [1–3]). Since then, the interplay between topology and correlation has been the primary focus of condensed matter research. Graphene and its variants, due to its excellent electronic and mechanical properties [4, 5], have become wonderful platforms for hosting exotic phases of matter and also find themselves widely applicable in electric device engineering and material science. The characteristic feature of graphene is the appearance of the Dirac cone in the spectrum, closely tied to the symmetry of the underlying honeycomb lattice. The two sublattices (A and B) of the honeycomb lattice transform into each other under the simplest non-abelian point group  $C_{3v}$ , which contains 3-fold rotations and in-plane reflections. At the  $K(K')$  point of the Brillouin zone, the wave functions of A and B sublattices form the two-dimensional ( $E$ ) irreducible representations (irrep) of the  $C_{3v}$ , enforcing the Dirac cones. Once there, the Dirac cones are stable as long as the time-reversal and inversion symmetry are preserved.

The on-site  $p_z$  orbital of graphene transforms trivially (it belongs to the  $A_1$  irrep) under the site symmetry group  $C_{3v}$ . It is natural to ask what happens if the on-site orbitals form the  $E$  irrep of the point group. The  $E$  irrep features double degeneracy and strong anisotropy and is expected to bring rich orbital physics in graphene-like Dirac materials. Such a situation arises in many distinct systems. It was initially studied in optical lattices, where the two-dimension irrep is realized by the  $p_x$  and  $p_y$  orbitals in the harmonic trap [6, 7]. In the transition metal oxide heterostructures [8–10] and transition metal dichalcogenide monolayers [11], the  $d$  orbitals of the tran-

sition metal decompose based on the  $C_{3v}$  symmetry and are active near the Fermi surface. In hexagonal monolayers of heavy elements, such as Germanene, Stanene, and Bismuthene, the  $(p_x, p_y)$  doublets realize the orbital degrees of freedom and because of the large atomic spin-orbit coupling, contribute to the large topological gaps [12–17]. Even in simple carbon systems, orbital physics can be realized via lattice engineering, for example, organic framework [18, 19] and graphene-kagome lattice [20]. Remarkably, recently experiments [21–23] on twisted bilayer graphene revealed Mott insulator and superconductivity phases, and it is proposed that the low-lying degrees of freedom are compatible with two orbitals on the honeycomb lattice as well [24–29]. Furthermore, the orbital degrees of freedom do not have to be electronic and can manifest themselves as the polarization modes of polaritons in photonic lattices [30, 31] and phonons in graphene and mechanical structures [32–35].

Given all these interconnected systems and the increasing new realizations of orbital-active Dirac material, this work aims to bridge all the different systems through the symmetry principle. Despite the vastly different origins, the orbital degrees of freedom can be understood as the irreducible representations of the site symmetry of the lattice, which can lead to universal properties. We show that the symmetry alone enforces the Dirac cone at  $K(K')$  point and the quadratic band touching at the  $\Gamma$  point. We further discuss various gap opening mechanisms and interaction effects, which lead to the quantum spin Hall effect and quantum anomalous Hall effect. In particular, when the  $E_g$  doublets realize orbital degrees of freedom, the resulting topological insulator states carry octupole order. Finally, the method we use here to study the doubly-degenerate orbitals in the honeycomb lattice can be readily generalized to the orbital degrees of freedom arising from larger point groups on lattices described

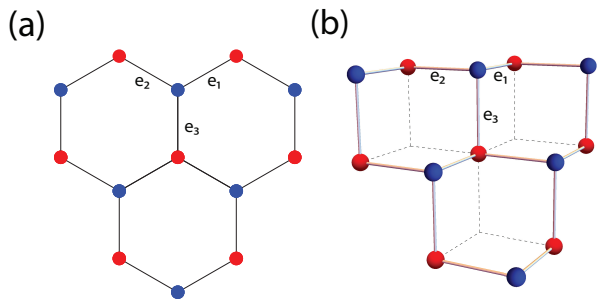


FIG. 1. (a) The standard honeycomb lattice with  $C_{6v}$  point symmetry group. (b) The buckled honeycomb lattice with the symmetry group is downgraded to  $D_{3d}$ .

by other space groups. The rest of the paper is organized as follows. In Sec. II, we discuss the symmetry of the honeycomb lattice and the orbital realization of the on-site irreducible representations, focusing on the  $d$  orbitals. In Sec. IV, we derive the band structure of the orbital-active honeycomb lattice systems from a simple tight-binding model. In Sec. V, we go beyond the simple tight-binding model and demonstrate that many interesting features of the band structure are solely protected by the lattice symmetry. In Sec. VI, we investigate various band gap opening mechanisms. In Sec. VII, the interplay between the band structure and the interaction effects is discussed. Sec. VIII is left for summary and outlook.

## II. THE HONEYCOMB LATTICE AND ORBITAL SYMMETRIES

We start with reviewing the symmetry of the planar honeycomb lattice. The planar honeycomb lattice, sketched in in Fig. 1(a), consists of two sublattices  $A$  (blue) and  $B$  (red). The three nearest neighbor vectors are labeled as  $\hat{e}_1 \sim \hat{e}_3$ . The symmetry of the lattice is described by the space group  $P6mm$ , a direct product of the point group  $C_{6v}$  and the translation symmetry of the triangular Bravais lattice<sup>1</sup>. The maximal point group  $C_{6v}$  is realized at the centers of the hexagons. On the other hand, the point group symmetry acting on a lattice site, called site symmetry, is a subgroup of the maximal point group. The site symmetry group is important because it affects the orbital part of the wave function of the degrees of freedom living on lattice sites (such as electrons, phonons, etc.) The site symmetry of the honeycomb lattice is  $C_{3v}$  generated by a 3-fold rotation axis and three vertical reflection planes (e.g., the  $yz$ -plane and its symmetry counterparts by rotations of  $\pm 120^\circ$ ). In contrast, the reflection with respect to the  $xz$ -plane and its symmetry counterparts by rotations of

$\pm 120^\circ$  interchange the  $A$  and  $B$  sublattices and are not included in the site symmetry.

The orbital of the onsite degrees of freedom is classified by the irreducible representations of the site symmetry group. The  $C_{3v}$  group has three irreducible representations (irrep), including two 1d irreps  $A_{1,2}$  and a 2d irrep  $E$  as explained in Appendix A. The irreps fully determines the symmetry structure of the onsite degrees of freedom, regardless of their microscopic origins. In this paper, we mainly focus on electron atomic orbitals. Taking  $z$  axis perpendicular to the lattice plane, the  $s$  and  $p_z$  orbitals realize the  $A_1$  irrep and lead to the remarkable electronic structure of graphene. In contrast, the  $p_x$  and  $p_y$  orbitals realize the two dimensional  $E$  irrep. This doublet can also be organized into the complex basis  $p_x \pm ip_y$  which are eigenstates of the orbital angular momentum  $L_z$  with eigenvalues  $\pm 1$ , respectively. As to the 5-fold  $d$ -orbitals, the  $d_{r^2-3z^2}$  falls into the  $A_1$  irrep. The remaining four form two  $E$  irreps: the  $(d_{xz}, d_{yz})$  doublet and the  $(d_{xy}, d_{x^2-y^2})$  doublet. The complex orbitals  $d_{xz} \pm id_{yz}$ , and  $d_{xy} \pm d_{x^2-y^2}$  carry orbital angular momentum numbers  $\pm 1$  and  $\mp 2$  respectively. Since the site symmetry group only has one 2d irrep, the three doublets,  $(p_x, p_y)$ ,  $(d_{xz}, d_{yz})$  and  $(d_{xy}, d_{x^2-y^2})$  are equivalent as far as the symmetry is concerned. One can explicitly check that the group elements of the site symmetry  $C_{3v}$  have the same matrix representation in the basis of all realizations of the  $E$  irrep.

We consider a closely related lattice structure sketched in Fig 1(b). This lattice structure, dubbed buckled honeycomb lattice, can be viewed as a bilayer of sites taken from a cubic lattice in the  $(1, 1, 1)$  direction. The blue and red dots form a honeycomb lattice when projecting into the  $(1, 1, 1)$  plane. Compared to the planar honeycomb lattice, the point group symmetry of the buckled lattice downgrades from  $d_{6h}$  to  $d_{3d}$ , where the six-fold rotation becomes a rotoinversion. On the other hand, the site symmetry remains the same, described by  $C_{3v}$ . As a result, based on previous analysis, the realizations of the  $E$  irrep in the buckled lattice must be equivalent to the  $(p_x, p_y)$  doublet in the planar case. Here we focus on the  $d$  orbitals and establish this equivalence. The buckled honeycomb lattice originates from the cubic lattice. Taking the  $z$  along  $(0, 0, 1)$ , the 5-fold  $d$  orbitals split into a  $T_{2g}$  triplet  $(d_{yz}, d_{zx}, d_{xy})$  and a  $E_g$  doublet  $(d_{x^2-y^2}, d_{r^2-3z^2})$ , which are irreps of the  $O_h$  point group. The site symmetry of the buckled lattice  $C_{3v}$  is a subgroup of  $O_h$ . The  $E_g$  doublet falls into the only 2d irrep  $E$  of  $C_{3v}$ , while the  $T_{2g}$  triplet further splits into the 1d irrep  $A_1$  and the 2d irrep  $E$ . To make the connection between the  $E_g$  doublet and the orbital realization of the  $E$  irrep in the planar case more explicit, we can rotate the frame of the buckled lattice so that the  $z$  axis is along the 3-fold rotation axis  $(1, 1, 1)$ . Under this frame rotation, the  $E_g$  doublet

<sup>1</sup> If one also considers the mirror symmetry taking  $z$  to  $-z$ , the point group is  $D_{6h}$  and the space group is  $P6/mmm$ .

becomes

$$\begin{aligned} d_{x^2-y^2} &\rightarrow \frac{1}{\sqrt{3}}(d_{xy} + \sqrt{2}d_{xz}), \\ d_{r^2-3z^2} &\rightarrow \frac{1}{\sqrt{3}}(d_{x^2-y^2} + \sqrt{2}d_{yz}). \end{aligned} \quad (1)$$

Hence, the  $E_g$  orbitals are a superposition of two  $E$  doublets  $(d_{xy}, d_{x^2-y^2})$  and  $(d_{xz}, d_{yz})$  in the planar case. Therefore, as far as the site symmetry  $C_{3v}$  is concerned, the  $e_g$  doublet is equivalent to the  $(p_x, p_y)$  doublet in the planar case with the following mapping,

$$d_{x^2-y^2} \leftrightarrow p_x, \quad d_{r^2-3z^2} \leftrightarrow p_y. \quad (2)$$

For completeness, we present the decomposition of the five  $d$ -orbitals into two  $E$  irreps and one  $A_1$  irrep of the  $C_{3v}$  group as follows,

$$\begin{cases} (d_{x^2-y^2}, d_{r^2-3z^2}) & E \\ \left( \frac{1}{\sqrt{2}}(d_{yz} - d_{zx}), \frac{1}{\sqrt{6}}(d_{yz} + d_{zx} - 2d_{xy}) \right) & E \\ \frac{1}{\sqrt{3}}(d_{xy} + d_{yz} + d_{zx}) & A_1, \end{cases} \quad (3)$$

choosing  $(1, 1, 1)$  as the rotation axis. In addition to the  $E_g$  orbitals which become an  $E$ -representation, the  $T_{2g}$ -orbitals split into one  $E$  irrep and one  $A_1$  irrep. In principle, the two  $E$ -representations from the  $E_g$  and  $T_{2g}$  orbitals can mix. In transition metal oxide where the buckled lattice is relevant, there is often an oxygen octahedron around each transition metal ion. The oxygen octahedron introduces a large crystal field that splits the  $E_g$  and  $T_{2g}$  orbitals. As a result, the mixing between the  $E$  irrep of  $C_{3v}$  derived from the  $E_g$  orbitals and that from the  $T_{2g}$  orbitals is weak.

### III. MAGNETIC OCTUPOLE MOMENT OF THE $E_g$ DOUBLET

Although all realizations of  $E$  irrep of  $C_{3v}$  are equivalent from the symmetry consideration. The  $E_g$  orbitals are special physically and worth special attention. The key difference lies in the angular momentum of the complex combination of the doublets. In the case of  $(p_x, p_y)$ , the complex combination  $p_x \pm ip_y$  takes the form  $\exp(\pm i\theta)$ , and thus carry angular momentum  $\pm 1$  along the rotating axis. The same applies to the  $(d_{xz}, d_{yz})$  doublet. In the case of  $(d_{xy}, d_{x^2-y^2})$ , the complex combination  $d_{xy} \pm id_{x^2-y^2}$  takes the form  $\exp(\mp i2\theta)$  and thus carries angular momentum  $\mp 2$ . In contrast, the angular momentum of the complex combination of the  $E_g$  orbitals  $d_{x^2-y^2} \pm d_{r^2-3z^2}$  vanishes. From Eq. (1), the complex combination of  $E_g$  doublet can be viewed as the weighted superposition of the complex combinations of the  $(d_{xz}, d_{yz})$  and  $(d_{xy}, d_{x^2-y^2})$ . The angular momentum of the two doublets cancel each other, leading to the zero angular momentum of the  $E_g$  doublet.

Instead of angular momentum, the complex  $E_g$  orbitals carry higher rank magnetic momentum, measured

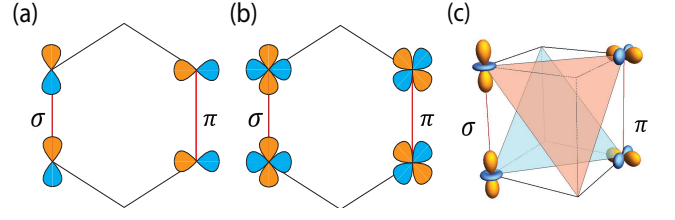


FIG. 2. The orbital configuration of the  $\sigma$ -bonding on the  $\hat{e}_3$  bond for (a)  $(p_x, p_y)$  doublet; (b)  $(d_{xy}, d_{x^2-y^2})$  doublet; (c)  $E_g$  doublets.

by spherical tensor operators  $Y_{lm}$ . A list of spherical tensor operators constructed from the angular momentum operator  $\vec{L}$  in the  $d$  orbital space can be found in appendix B. Going through all the higher rank tensor operators, we find that the leading non-vanishing spherical tensor operators projecting into  $E_g$  orbital is

$$P_{E_g} Y_{3,\pm 2} P_{E_g} = \mp 3\sqrt{\frac{5}{2}} i\sigma_2 \quad (4)$$

where  $P_{E_g}$  is the projection operator. The two non-vanishing components of the rank 3 spherical tensor operators can be grouped into a single cubic harmonic tensor  $\hat{f}_{xyz} = \frac{i}{\sqrt{2}}(Y_{2,-2} - Y_{2,2})$ , which is projected into  $E_g$  orbital space as

$$P_{E_g} \hat{f}_{xyz} P_{E_g} = -3\sqrt{5}\sigma_2. \quad (5)$$

where  $\hat{f}_{xyz}$  corresponds to the octupole magnetic moment. Therefore, the complex combinations of the  $E_g$  orbital, instead of carrying angular momentum, carry octupole magnetic moment, which was proposed to be the “hidden order” in certain strongly-correlated electronic systems [36–40].

### IV. THE BAND STRUCTURE OF THE ORBITAL ACTIVE HONEYCOMB LATTICE

In this section, we study the band structure arising from the orbital degrees of freedom on the planar and the buckled honeycomb lattice. To be concrete, we first introduce a simple nearest neighboring tight-binding model before presenting more general scenarios in the next section.

#### A. Constructing the tight-binding model

In the orbital active honeycomb lattice, the hopping between neighboring sites occurs between different components of the  $E$  irrep and thus is more complicated than the orbital inactive case. There are two kinds of hopping processes allowed by symmetry on a bond. In the convention of chemistry, the one with larger hopping amplitude is called  $\sigma$  bonding, and the other one is called  $\pi$

bonding. The difference in the hopping amplitude arises from the anisotropy of the orbital wave function. The bonding direction of the  $\sigma$  ( $\pi$ ) bond is along the direction of the maximal (minimal) angular distribution of orbital wave functions. The  $\sigma$  bond and the  $\pi$  bond for all orbital realizations of the  $E$  irrep are shown in Fig. 2 for one of nearest neighboring bond  $\hat{e}_3$ . In the planar case, the  $\sigma$  bonding orbital is  $p_y$ ,  $d_{yz}$  or  $d_{x^2-y^2}$ , and in the buckled case, the  $\sigma$  bonding orbital is  $d_{r^2-3z^2}$ . The  $\sigma$  bonding orbitals along other nearest neighboring bond are linear combinations of the two orbitals in the  $E$  irrep, obtained from applying 3 fold rotation on  $p_y$ ,  $d_{yz}$ ,  $d_{x^2-y^2}$  or  $d_{r^2-3z^2}$ . Since all the different doublets form the same irrep of  $C_{3v}$  point group, they transform in the same way under rotation. To unify the notation, we use  $\gamma_{x,y}$  to represent the two states in the  $E$  irrep for different orbital realizations, where  $\gamma_x$  stands for  $p_x$ ,  $d_{xy}$  or  $d_{x^2-y^2}$ , and  $\gamma_y$  stands for  $p_y$ ,  $d_{x^2-y^2}$  or  $d_{r^2-3z^2}$  correspondingly. We define  $\gamma_1 \sim \gamma_3$  to be the  $\sigma$  bonding orbitals along the three nearest neighboring bonds  $\hat{e}_1 \sim \hat{e}_3$ ,

$$\gamma_1 = \frac{\sqrt{3}}{2}\gamma_x + \frac{1}{2}\gamma_y, \quad \gamma_2 = -\frac{\sqrt{3}}{2}\gamma_x + \frac{1}{2}\gamma_y, \quad \gamma_3 = -\gamma_y. \quad (6)$$

Since the  $\sigma$  bonding is much stronger than the  $\pi$  bonding, we neglect the  $\pi$  bonding and construct the single particle Hamiltonian of the nearest neighboring  $\sigma$  bonding. Using  $\gamma_1 \sim \gamma_3$ , the Hamiltonian can be conveniently written as

$$H_0 = t_{\parallel} \sum_{\vec{r} \in A, j=1,2,3} \left\{ \gamma_j^{\dagger}(\vec{r} + \hat{e}_j) \gamma_j(\vec{r}) + h.c. \right\}. \quad (7)$$

where the summation over  $\vec{r}$  is only on the A sublattice and  $\hat{e}_1 \sim \hat{e}_3$  are the unit vectors pointing from A site to its three nearest neighboring B sites on the planar honeycomb lattice

$$\hat{e}_1 = \frac{\sqrt{3}}{2}\hat{e}_x + \frac{1}{2}\hat{e}_y, \quad \hat{e}_2 = -\frac{\sqrt{3}}{2}\hat{e}_x + \frac{1}{2}\hat{e}_y, \quad \hat{e}_3 = -\hat{e}_y. \quad (8)$$

We have set the nearest neighboring distance to 1. In the case of the buckled honeycomb lattice, the three nearest neighboring vectors are the same as in the planar case when the coordinates are projected onto the  $(1, 1, 1)$  plane. The Hamiltonian has the same form for different realizations of the  $E$  irrep of the site symmetry  $C_{3v}$  for both the planar and buckled honeycomb lattice. This demonstrates the power and elegance of the symmetry principle.

## B. The spectrum and wavefunctions

The Hamiltonian Eq. (7) is ready to be diagonalized in the momentum space. We define a 4-component spinor  $\psi(\vec{k})$  in momentum space as

$$\psi(\vec{k}) = (\gamma_{x,A}(\vec{k}), \gamma_{y,A}(\vec{k}), \gamma_{x,B}(\vec{k}), \gamma_{y,B}(\vec{k}))^T, \quad (9)$$

where  $A$  and  $B$  refer to the two sublattices. The annihilation operators  $\gamma_{x,y}(\vec{k})$  is defined as

$$\gamma_{x,y}(\vec{k}) = \frac{1}{\sqrt{N}} \sum_{\vec{r}} \gamma_{x,y}(\vec{r}) e^{-i\vec{k} \cdot \vec{r}}, \quad (10)$$

The crystal momentum  $\vec{k}$  is defined in the Brillouin zone shown in Fig. 3(a). In the case of the buckled honeycomb lattice,  $\vec{r}$  is the projected coordinate in the  $(1, 1, 1)$  plane.

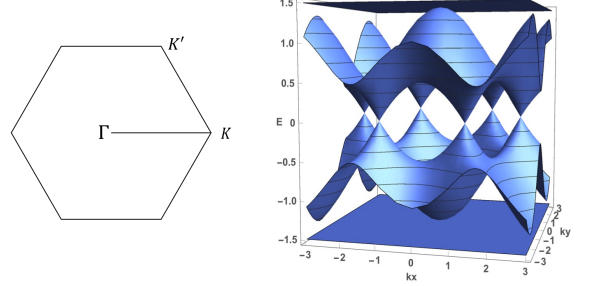


FIG. 3. (a) The Brillouin zone of the honeycomb lattice. (b) The band structure of the tight binding model is described in Eq. (7) in the strong anisotropy limit. There are four bands (The spin degrees of freedom just add another copy and are omitted). The bottom band and the top band are completely flat, while the middle two bands have the same dispersion relations as in graphene.

With this setup, the Hamiltonian takes the following block form:

$$H(\vec{k}) = \begin{pmatrix} 0 & H_{AB} \\ H_{AB}^{\dagger} & 0 \end{pmatrix}, \quad (11)$$

where

$$H_{AB} = t_{\parallel} \begin{pmatrix} \frac{3}{4}(e^{i\vec{k} \cdot \hat{e}_1} + e^{i\vec{k} \cdot \hat{e}_2}) & \frac{\sqrt{3}}{4}(e^{i\vec{k} \cdot \hat{e}_1} + e^{i\vec{k} \cdot \hat{e}_2}) \\ \frac{\sqrt{3}}{4}(e^{i\vec{k} \cdot \hat{e}_1} + e^{i\vec{k} \cdot \hat{e}_2}) & \frac{1}{4}(e^{i\vec{k} \cdot \hat{e}_1} + e^{i\vec{k} \cdot \hat{e}_2} + 2e^{i\vec{k} \cdot \hat{e}_3}) \end{pmatrix}. \quad (12)$$

There are four bands in total. The middle two bands have the exact dispersion as that in graphene:

$$E_{2,3} = \mp \frac{t_{\parallel}}{2} \left| \sum_i e^{i\vec{k} \cdot \hat{e}_i} \right| = \mp \frac{t_{\parallel}}{2} \sqrt{3 + 2 \sum_{i=1}^3 \cos \vec{k} \cdot \vec{b}_i}, \quad (13)$$

where  $\vec{b}_i = \frac{1}{2}\epsilon_{ijk}(\hat{e}_j - \hat{e}_k)$  are the next nearest neighboring vectors. The bands display two Dirac cones at  $K$  and  $K'$ . In addition, Fermi surface nesting and Van Hove singularity occur at  $1/4$  filling above and below the Dirac point. The wave functions associated with the middle two bands are

$$|\psi(\vec{k})\rangle_{2,3} = \frac{1}{\sqrt{N_0}} \left( e^{-i\frac{\theta}{2}} \sum_i \hat{e}_i e^{i\vec{k} \cdot \hat{e}_i}, \pm e^{i\frac{\theta}{2}} \sum_i \hat{e}_i e^{-i\vec{k} \cdot \hat{e}_i} \right), \quad (14)$$



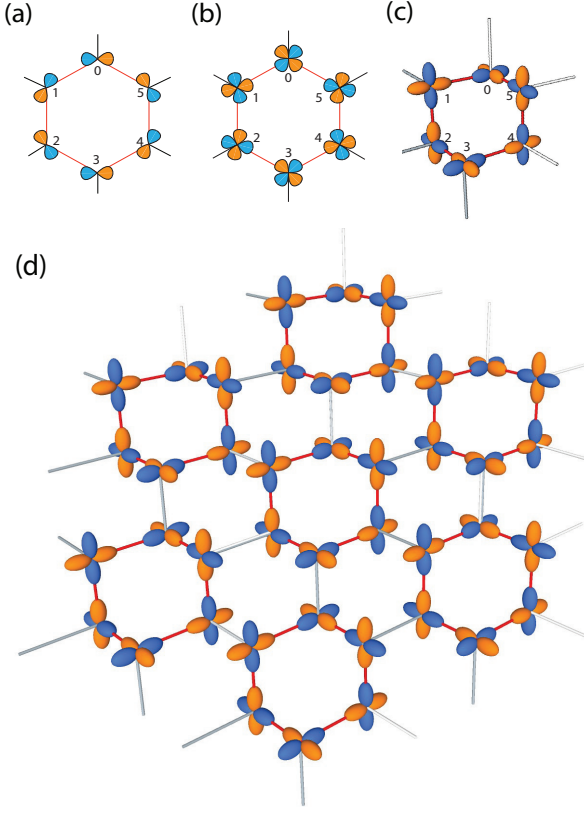


FIG. 4. (a) The spatial localized states in the lower flat band of the tight-binding Hamiltonian Eq. (7) for (a)  $(p_x, p_y)$  doublet; (b)  $(d_{xz}, d_{yz})$  doublet; (c)  $E_g$  doublet. (d) The spatial localized state Wigner-crystal when the lower flat-band is 1/3 filled.

where the phase  $\theta = \arg(\sum_i e^{i\vec{k} \cdot \vec{e}_i})$  and the normalization

$$N_0 = 6 - 2 \sum_{i=1}^3 \cos \vec{k} \cdot \vec{b}_i.$$

On the other hand, the top band and the bottom band are perfectly flat with the energy

$$E_{1,4} = \mp \frac{3}{2} t_{\parallel} \quad (15)$$

and connect to the middle two bands at the  $\Gamma$  point. The corresponding wave functions are

$$|\psi(\vec{k})\rangle_{1,4} = \frac{1}{\sqrt{3N_0}} \left( \sum_i \vec{b}_i e^{-i\vec{k} \cdot \vec{e}_i}, \pm \sum_i \vec{b}_i e^{i\vec{k} \cdot \vec{e}_i} \right). \quad (16)$$

The entire spectrum is plotted in Fig. 3.

### C. The appearance of the flat-band and the localized state

The existence of the flat bands implies that one can construct a local eigenstate of the single-particle Hamiltonian. The flat band has been studied in detail in [6, 7]

in the context of the  $p$  orbitals in the honeycomb optical lattice, and plaquette states on a hexagon are constructed as the local basis (Fig. 4(a)). Here we investigate it in the orbital-active Dirac material realized by the  $(d_{xy}, d_{x^2-y^2})$  and the  $e_g$  doublets.

The localized states can be elegantly constructed from the Bloch wave function in Eq. (16),

$$|\psi_{\vec{R}}\rangle_{\pm} = \frac{1}{\sqrt{N_k}} \sum_k |\psi(\vec{k})\rangle_{1,4} e^{-i\vec{k} \cdot \vec{R}}, \quad (17)$$

where  $\vec{R}$  are the centers of the hexagons. Each hexagon hosts one localized state from each flat band. The localized states are

$$|\psi_{\vec{R}}\rangle_{\pm} = \sum_{n=0}^5 (\pm 1)^n \left( \cos \frac{n\pi}{3} \gamma_x^\dagger(\vec{r}_n) + \sin \frac{n\pi}{3} \gamma_y^\dagger(\vec{r}_n) \right) |0\rangle. \quad (18)$$

The summation is over the six vertices of the hexagon as shown in Fig. 4(b) for the case of the  $(d_{xy}, d_{x^2-y^2})$  doublet. The localized state has the same weight on each site but different orbital configurations, related by  $\frac{\pi}{3}$  rotations. On each site, the orbital is projected into the  $\pi$ -bonding along the outward bond away from the hexagon. Due to the destructive interference, electrons in such localized single-particle states cannot leak out the plaquette, rendering the localized states eigenstates of the tight-binding Hamiltonian in Eq. (7) with the same energy. The above analysis can be carried over to the  $E_g$  doublets on the buckled honeycomb lattice. In this case, the localized state is confined in a buckled hexagon as shown in Fig. 4(c).

### D. Orbital configurations at high symmetric points

As shown in Fig. 3(b), the spectrum exhibits double degeneracy at the  $K(K')$  point and the  $\Gamma$  point in the Brillouin zone. Now we investigate the Bloch wave function at these high symmetric points in detail.

#### 1. $\Gamma$ point

Around the center of the Brillouin zone  $\vec{k} = (0, 0)$ , the Hamiltonian Eq. (11), in the unit of  $t_{\parallel}$ , can be expanded as

$$H_{\Gamma}(k) = \frac{3}{2} \left( 1 - \frac{1}{4} |k|^2 \right) \tau_1 \otimes \sigma_0 - \frac{3}{4} (k_x \tau_2 \otimes \sigma_1 + k_y \tau_2 \otimes \sigma_3) - \frac{3}{16} ((k_x^2 - k_y^2) \tau_1 \otimes \sigma_3 + 2k_x k_y \tau_1 \otimes \sigma_1), \quad (19)$$

where the Pauli matrices  $\sigma_0 \sim \sigma_3$  ( $\sigma_0$  represents the identity matrix) describe the orbital degrees of freedom  $\gamma_{x,y}$  in the  $E$  irrep, and  $\tau_0 \sim \tau_3$  act on the space of sublattice

$(A, B)$ . To the leading order, the dispersion of the bands is

$$\begin{aligned} E_{1,4}^\Gamma &= \mp \frac{3}{2} t_\parallel \\ E_{2,3}^\Gamma &= \pm \frac{3}{2} t_\parallel \left( -1 + \frac{1}{4} |\Delta k|^2 \right). \end{aligned} \quad (20)$$

Therefore, the bands touch each other quadratically at both upper and lower degeneracy points. The degenerate wave functions at each touching point can be regrouped so that they only contain one of each the orbital component. At the lower touching point, the wave functions are

$$|\psi(\Gamma)\rangle_{x(y)}^+ = \frac{1}{\sqrt{2}} \left( \gamma_{x(y),A}^\dagger + \gamma_{x(y),B}^\dagger \right) |0\rangle. \quad (21)$$

At the upper touching point, the  $B$  sublattice component acquires a minus sign, and the wave functions are

$$|\psi(\Gamma)\rangle_{x(y)}^- = \frac{1}{\sqrt{2}} \left( \gamma_{x(y),A}^\dagger - \gamma_{x(y),B}^\dagger \right) |0\rangle. \quad (22)$$

## 2. $K$ and $K'$ points

Around  $\vec{K} = (\frac{4\pi}{3\sqrt{3}}, 0)$ , the Hamiltonian in Eq. (11) can be expanded as

$$\begin{aligned} H_K &= -\frac{4}{3} \Delta k_x \tau_1 \otimes \sigma_0 + \frac{4}{3} \Delta k_y \tau_2 \otimes \sigma_0 \\ &\quad - \frac{3}{8} (2 + \Delta k_x) \tau_1 \otimes \sigma_0 - \frac{3}{8} \Delta k_y \tau_2 \otimes \sigma_3 \\ &\quad - \frac{3}{8} \Delta k_y \tau_1 \otimes \sigma_1 - \frac{3}{8} (2 - \Delta k_x) \tau_2 \otimes \sigma_1, \end{aligned} \quad (23)$$

where  $\Delta \vec{k} = \vec{k} - \vec{K}$ . The middle two bands touch each other with the dispersion,

$$E_{2,3} = \mp \frac{3}{4} t_\parallel |\Delta k|, \quad (24)$$

which demonstrates the Dirac cone. The doubly degenerate wave functions can be combined so that each of them only occupies one of the sublattices:

$$\begin{aligned} |\psi(\vec{K})\rangle_A &= \frac{1}{\sqrt{2}} \left( \gamma_{x,A}^\dagger + i \gamma_{y,A}^\dagger \right) |0\rangle \\ |\psi(\vec{K})\rangle_B &= \frac{1}{\sqrt{2}} \left( \gamma_{x,B}^\dagger - i \gamma_{y,B}^\dagger \right) |0\rangle. \end{aligned} \quad (25)$$

The orbital states on the two sublattices are circular polarized and exhibit opposite chiralities. Such complex combinations of the orbitals exhibit distinct physical properties for different orbital realizations. In the case of the  $(p_x, p_y)$  doublet as well as the  $(d_{xz}, d_{yz})$  doublet, the circular polarized state  $|\gamma_1\rangle \pm i |\gamma_2\rangle$  carries angular momentum  $L_z = \pm 1$ ; in the case of the  $(d_{xy}, d_{x^2-y^2})$  doublet, the circular polarized state carries angular momentum  $\mp 2$ ; in the case of the  $E_g$  doublet, it carries magnetic octupole moment. These complex orbital states play an important role in the topological properties of the orbital-active Dirac material and will be addressed in Sec. VI.

## E. Response of the flat band to magnetic field

One interesting question regarding the flat band that appeared is its response to an external magnetic field. In a flat band, because the kinetic energy of the electrons is completely quenched, the usual semi-classical picture is no longer valid. Recent work [41] demonstrates that the response of flat bands to an external magnetic field is closely related to the quantum distance of the flat band. The quantum distance between two Bloch wavefunctions is defined as,

$$d = 1 - |\langle \psi(k) | \psi(k') \rangle|^2, \quad (26)$$

which ranges from 0 to 1. The flat band is singular if  $d$  is nonzero in the limit that  $|k - k'| \rightarrow 0$ . A singular point  $k_0$  can be characterized by the maximal quantum distance  $d_{max}$  between the wavefunctions of  $k$  and  $k'$  that are sufficiently close to  $k_0$ . In systems without orbital degrees of freedom, it is found that when  $d_{max}$  is nonzero, the flat band splits into Landau levels in an energy window, and the width of the energy window is determined by  $d_{max}$ .

In our case, the flat band touches the dispersive Dirac band at the  $\Gamma$  point. The wavefunction of the flat band, expanded around the  $\Gamma$  point, is

$$|\psi\rangle = \frac{1}{\sqrt{2}} \left( \sin \theta(\vec{k}), -\cos \theta(\vec{k}), \sin \theta(\vec{k}), -\cos \theta(\vec{k}) \right) \quad (27)$$

where  $\theta(\vec{k})$  is the azimuth angle of  $\vec{k}$ . Therefore, the wavefunction at  $\theta$  and  $\theta - \pi/2$  are orthogonal to each other, rendering the maximal quantum distance  $d = 1$ . As a result, the flat band that appeared here is singular by definition.

We study the response of the flat band to an external magnetic field by including the gauge field in the hopping parameter  $t \rightarrow t \exp(i \int A(\vec{r}) d\vec{r})$ . For simplicity, we choose the Landau gauge  $A = B(0, x)$  and the strength of the magnetic field  $B$  is set by the flux through each hexagon  $2\pi p/q$ . In the presence of the magnetic field, the original four bands split into  $4q$  sub-bands. The band structure is shown in Fig. 5. While the middle two dispersive Dirac bands form the characteristic Landau levels, surprisingly, the two singular flat bands are completely inert to the magnetic field, in contrast with previous results on singular flat bands without orbital degrees of freedom. This is due to the orbital nature of the singularity in Eq. (27). In the presence of the magnetic field, one can still construct localized states from the Bloch wavefunction of the flat band. Instead of occupying a hexagon, the localized states now occupy a magnetic unit cell. The wavefunction is nonzero only on the boundary of the magnetic unit cell, and the orbital configuration is parallel to the tangential direction. An example of the localized states is shown in Fig. 5(b) for the flux given by  $2\pi/3$ .

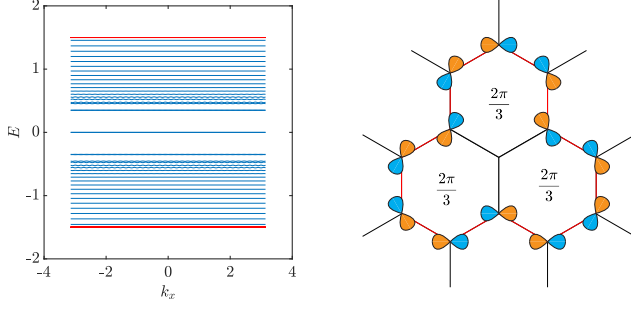


FIG. 5. (a) The flat band in the orbital active Dirac system is singular but does not respond to an external magnetic field due to the orbital nature of the singularity. (b) An example of the localized state in the presence of the magnetic field. Here the flux through each hexagon is  $2\pi/3$ . The localized state occupies three hexagons.

## V. GENERAL SYMMETRY CONSIDERATION BEYOND STRONG ANISOTROPIC LIMIT

In the last section, we demonstrate many remarkable features resulting from the tight-binding Hamiltonian Eq. (7), including orbital enriched Dirac cone, quadratic band touching and flat bands. Since the Hamiltonian only includes nearest neighboring hopping and  $\sigma$  bonding, a natural question is whether these features rely on the specific form of the Hamiltonian or are generic results from the symmetry.

In this section, we address this issue by general symmetry consideration. We study the band structure of the orbital active Dirac materials around the high symmetric points in the Brillouin zone using  $k \cdot p$  theory. In summary, the band flatness is not generic and can be bent by the  $\pi$ -bondings, for example. However, the orbital configurations at the high symmetric points and  $k$  dependence of the dispersion around the  $\Gamma$  and  $K$  points are preserved as long as the symmetry of the system is respected. In the following, we consider the effects of the point group symmetry of the buckled honeycomb lattice  $D_{3d}$ .

### A. $\Gamma$ point

At the  $\Gamma$  point, the little group is the maximal point group of the lattice,  $D_{3d}$ . The Bloch wave function is composed of the orbital part  $|\gamma_{x,y}\rangle$  and the plane wave part  $|\Gamma\rangle_{A,B}$ , which can be classified into the irreps of the

little group separately. The orbital degrees of freedom ( $|\gamma_x\rangle, |\gamma_y\rangle$ ) form the two dimensional  $E_g$  irrep, while the plane wave part  $|\Gamma\rangle_A + |\Gamma\rangle_B$  and  $|\Gamma\rangle_A - |\Gamma\rangle_B$  form the one dimensional  $A_{1g}$  and  $A_{2u}$  irreps. Therefore the composite Bloch wave function can be grouped into two two-dimensional irreps,  $E_g$  and  $E_u$ , respectively. This indicates that the four energy levels can be grouped into two doubly-degenerate sets, where the degeneracy completely originates from the orbitals. The Bloch wave functions of the  $E_g$  irrep are

$$|\gamma_{x(y)}\rangle \otimes (|\Gamma\rangle_A + |\Gamma\rangle_B), \quad (28)$$

and wave functions of the  $E_u$  irrep are

$$|\gamma_{x(y)}\rangle \otimes (|\Gamma\rangle_A - |\Gamma\rangle_B), \quad (29)$$

This is consistent with Eq. (21) and Eq. (22). Furthermore, in both degeneracy sets, the orbital part of the wave functions can be regrouped into the complex orbital states  $|\gamma_{\pm}\rangle = |\gamma_1\rangle \pm i|\gamma_2\rangle$ . Therefore, spin-orbit coupling is able to gap out the degeneracy.

The generic dispersion around the  $\Gamma$  point can be obtained from the  $k \cdot p$  theory. The  $k \cdot p$  Hamiltonian is invariant under the  $D_{3d}$  point group symmetry. In order to write down all the symmetry allowed terms, it is convenient to first classify the operators in the orbital space  $\vec{\sigma}$ , the operators in the sublattice space  $\vec{\tau}$  and the momentum  $\vec{k}$  into irreps of the point group  $D_{3d}$ . In the sublattice space, the classification is

$$\begin{cases} \tau_0, \tau_1 & A_{1g} \\ \tau_2, \tau_3 & A_{2u}. \end{cases} \quad (30)$$

In orbital space, the classification is

$$\begin{cases} \sigma_0, & A_{1g} \\ \sigma_2, & A_{2g} \\ (\sigma_1, \sigma_3), & E_g. \end{cases} \quad (31)$$

For the momentum, the classification is

$$\begin{cases} (k_x, k_y) & E_u \\ k_x^2 + k_y^2 & A_{1g} \\ (2k_x k_y, k_x^2 - k_y^2), & E_g. \end{cases} \quad (32)$$

Based on these classifications and the product table of the  $D_{3d}$  point group, the most general Hamiltonian takes the following form,

$$H_{\Gamma}(\vec{k}) = (h_1 + h_2(k_x^2 + k_y^2))\tau_1 \otimes \sigma_0 + k_x(h_3\tau_2 \otimes \sigma_1 + h_4\tau_3 \otimes \sigma_1) + k_y(h_3\tau_2 \otimes \sigma_3 + h_4\tau_3 \otimes \sigma_3) + (k_x^2 - k_y^2)(h_5\tau_0 \otimes \sigma_3 + h_6\tau_1 \otimes \sigma_3) + 2k_x k_y(h_5\tau_0 \otimes \sigma_1 + h_6\tau_1 \otimes \sigma_1), \quad (33)$$

where  $h_1 \sim h_6$  are constants with the unit of energy. We

will see later that at the first order of  $\vec{k}$ , the degeneracy is

still preserved, so we have to include second-order terms of  $\vec{k}$ . It recovers the tight-binding Hamiltonian around the  $\Gamma$  point presented in Eq. (19), when the  $h$ s are set to

$$\begin{aligned} h_1 &= -4h_2 = -2h_3 = -8h_6 = \frac{3}{2}t_{\parallel} \\ h_4 &= h_5 = 0, \end{aligned} \quad (34)$$

In the leading order, the dispersion is

$$\begin{aligned} E_{1,2} &= -h_1 - \left(2h_2 + \frac{h_3^2 + h_4^2}{h_1}\right) |k|^2 \pm (h_5 - h_6) |k|^2 \\ E_{3,4} &= h_1 + \left(2h_2 + \frac{h_3^2 + h_4^2}{h_1}\right) |k|^2 \pm (h_5 + h_6) |k|^2. \end{aligned} \quad (35)$$

At finite  $k$ , the degeneracy is lifted by

$$\begin{aligned} |E_1^{\Gamma} - E_2^{\Gamma}| &= \frac{m_-}{2} |k|^2 \\ |E_3^{\Gamma} - E_4^{\Gamma}| &= \frac{m_+}{2} |k|^2. \end{aligned} \quad (36)$$

where the effect mass  $m_{\pm} = 4|h_5 \pm h_6|$ . Therefore, the bands touch quadratically at both degenerate points. It is known that quadratic band touching is unstable to interaction and can lead to exotic phases such quantum Hall effect and nematicity [42].

### B. $K(K')$ point

At the  $K$  point, the little group is  $D_3$ , containing the three-fold rotations perpendicular to the plane and a two-fold rotation through the plane that interchanges the two sublattices. The Bloch wave functions  $|\psi(K)\rangle$ , containing both the planewave part and the orbital part, can be organized into irreps of the little group. The planewave part contains two sublattice components, forming the  $E$ -irrep, with the  $A/B$  sublattice component carrying chirality  $\pm 1$ . The on-site orbital degrees of freedom  $\gamma_x$  and  $\gamma_y$  also transform as the  $E$  irrep, the complex combination  $\gamma_x \pm i\gamma_y$  carrying the chirality  $\pm 1$ . Therefore, the

four composite wave functions can be decomposed into three irreps as  $2 \otimes 2 = 1 \oplus 1 \oplus 2$ . There are two trivial  $A_1$  representations, where the chiralities of the orbital and planewave cancel each other and an  $E$  irrep where the chiralities of the orbital and planewave add up. In general, the two  $A_1$  states do not have the same energy. In contrast, the two states in the  $E$  irrep are degenerate from symmetry and carry opposite chirality at the Dirac point. Explicitly, the two states are:

$$\begin{aligned} &(|\gamma_x\rangle + i|\gamma_y\rangle) \otimes |K\rangle_A \\ &(|\gamma_x\rangle - i|\gamma_y\rangle) \otimes |K\rangle_B. \end{aligned} \quad (37)$$

This is consistent with the wave functions of the tight-binding model at  $K$  in Eq. (25).

To obtain the generic dispersion around  $K(K')$ , we again employ the  $k \cdot p$  theory. The Hamiltonian around  $K$ , a combination of the plane wave, orbital, and sublattice has to be invariant under the  $C_{3v}$  point group. Following the same strategy, we first organize  $\vec{\sigma}$ ,  $\vec{\tau}$  and the momentum  $\Delta\vec{k} = \vec{k} - \vec{K}$  into irreps of the little group  $d_3$ . In the sublattice space, we have,

$$\begin{cases} \tau_0, & A_1 \\ \tau_3, & A_2 \\ (\tau_1, -\tau_2), & E. \end{cases} \quad (38)$$

In orbital space, we have,

$$\begin{cases} \sigma_0, & A_1 \\ \sigma_2, & A_2 \\ (\sigma_3, -\sigma_1), & E. \end{cases} \quad (39)$$

In addition, the momentum  $(\Delta k_x, \Delta k_y)$  belongs to the  $E$  irrep as well.

Therefore, based on the product table of  $D_3$  point group, the most general Hamiltonian, apart from an overall constant, reads,

$$\begin{aligned} H_K(\Delta\vec{k}) &= h_1\tau_3 \otimes \sigma_2 + h_2(\tau_1 \otimes \sigma_3 + \tau_2 \otimes \sigma_1) + \\ &\Delta k_x \{+h_3\tau_0 \otimes \sigma_3 + h_4\tau_1 \otimes \sigma_0 + h_5\tau_2 \otimes \sigma_2 + h_6\tau_3 \otimes \sigma_1 + h_7(\tau_1 \otimes \sigma_3 - \tau_2 \otimes \sigma_1)\} + \\ &\Delta k_y \{-h_3\tau_0 \otimes \sigma_1 - h_4\tau_2 \otimes \sigma_0 + h_5\tau_1 \otimes \sigma_2 + h_6\tau_3 \otimes \sigma_3 + h_7(\tau_2 \otimes \sigma_3 + \tau_1 \otimes \sigma_1)\}. \end{aligned} \quad (40)$$

The expansion of the  $\sigma$ -bonding Hamiltonian at  $K$  in Eq. (23) is a special case with

$$\begin{aligned} h_2 &= h_4 = 2h_7 = -\frac{3}{4}t_{\parallel} \\ h_1 &= h_3 = h_5 = h_6 = 0. \end{aligned} \quad (41)$$

In the general situation, at the leading order of  $\Delta\vec{k}$ , the

dispersions of the four bands read,

$$\begin{aligned} E_{1,4}^K &= -h_1 \pm 2h_2 + \mathcal{O}(|\Delta k|^2) \\ E_{2,3}^K &= h_1 \pm 2h_7|\Delta k| + \mathcal{O}(|\Delta k|^2), \end{aligned} \quad (42)$$

which is consistent with those given by the nearest-neighbor tight-binding model. The dispersion  $E_{2,3}^K$  is Dirac-like as long as  $h_7 \neq 0$ . The situation of the  $K'$



point can be obtained by performing the reflection symmetry with respect to the  $y$  axis.

The above analysis solely relies on the non-abelian nature of the point group and therefore is widely applicable to the orbital-active Dirac material, independent of the origin of the orbitals.

## VI. GAP OPENING MECHANISM

We have shown that the symmetry of the honeycomb lattice protects the degeneracy of the band structure at  $K(K')$  point and  $\Gamma$  point. The degenerate states form the 2-dimensional irrep of the little group at the high symmetry points. The degeneracy can be lifted by including various symmetry-breaking terms in the Hamiltonian, which introduces gaps at the Dirac point or/and the quadratic band touching point. The interplay of different symmetry-breaking terms can give rise to various topological band structures, rendering the orbital active Dirac system a flexible platform for realizing topological insulators with different edge-state properties. In this section, we discuss the gap opening mechanisms for different orbital doublets of the  $E$  irrep, previously studied in different contexts [8, 14], in a unified manner.

Based on Eq. (21) and Eq. (25), the degenerate wave functions at  $\Gamma$  and  $K$  can be grouped into circular polarized orbital state  $\gamma_x \pm i\gamma_y$  with opposite chirality. As a result, a  $\sigma_2$  term in the orbital space, which measures the chirality, is able to lift the degeneracy at both  $\Gamma$  and  $K$  points. In addition, at  $K(K')$  points, the two complex orbital states only occupy A and B sublattices, respectively. As a result, a  $\tau_3$  term in the sublattice space can also gap out the Dirac points. In contrast, since the degenerate states at the  $\Gamma$  point have the same weight on both sublattices, they remain degenerate after the  $\tau_3$  term is added to the Hamiltonian. One can also add other terms to the  $k \cdot p$  Hamiltonian to open up a gap in the spectrum. But the two terms mentioned above,  $\tau_3$  and  $\sigma_2$ , denoted as  $H_m$  and  $H_\lambda$  respectively, are among the simplest and have a clear physical origin. In the real space, they have the following form,

$$\begin{aligned} H_m &= m \left\{ \sum_{\vec{r} \in A, \sigma} \gamma_\sigma^\dagger(\vec{r}) \gamma_\sigma(\vec{r}) - \sum_{\vec{r} \in B, \tau} \gamma_\tau^\dagger(\vec{r}) \gamma_\tau(\vec{r}) \right\} \\ H_\lambda &= \lambda \left\{ \sum_{\vec{r} \in A, B} i\gamma_x^\dagger(\vec{r}) \gamma_y(\vec{r}) + h.c. \right\}. \end{aligned} \quad (43)$$

The term  $H_m$  represents the staggering mass resulting from the imbalance between the A and B sublattices, which for example, occurs in TMD materials. It only depends on the particle number on each sublattice and does not rely on the particular orbital state the electrons occupy. On the other hand,  $H_\lambda$  measures the chirality of the orbital and originates from spin-orbit coupling  $-\lambda_0 \vec{L} \cdot \vec{S}$ , where  $\lambda_0$  is the atomic spin-orbit coupling strength,  $\vec{L}$

is the physical angular momentum operator and  $\vec{S}$  is the spin operator of electrons.

In free space,  $\vec{L}$  acts on the Hilbert space labeled by the angular momentum  $S, p, d$ , etc. In the case of the planar and buckled honeycomb lattices, the spherical symmetry reduces to the site symmetry  $C_{3v}$ . As the result, the physical angular momentum  $\vec{L}$  should be projected into the 2d irrep. The result depends on the particular orbital realizations of the irrep, even though they are equivalent under the  $C_{3v}$  point group. In the following, we discuss the different orbital realizations case by case.

In the case of the  $(p_x, p_y)$  and  $(d_{xz}, d_{yz})$  doublets, the circular polarized orbital state have angular momentum  $\pm 1$ . The  $L_z$  operator, projecting into the two-dimensional space, becomes  $\sigma_2$ , while  $L_x$  and  $L_y$  are zero. The spin orbit coupling  $-\lambda \vec{L} \cdot \vec{S}$  becomes  $-\lambda \sigma_y s_z$ . As a result, after the spin-orbit coupling is included in the Hamiltonian, which lifts the degeneracy at the  $\Gamma$  point and the  $K$  points, the complex orbital state with positive chirality,  $p_x + ip_y$  or  $d_{xz} + id_{yz}$ , has higher energy than its partner, as shown in Fig. 6(a). In the case of the  $(d_{xy}, d_{x^2-y^2})$  doublet, the complex orbital states carry angular momentum  $\mp 2$ . The  $L_z$  operator in this space is  $-2\sigma_y$  while the other components vanish. Therefore, the spin-orbit coupling term is  $2\lambda_0 \sigma_y s_z$ . Note the factor of 2 and extra minus sign compared with the previous two cases. Therefore, the complex orbital state  $d_{xy} + id_{x^2-y^2}$  has lower energy than its partner at the  $\Gamma$  point and the  $K$  points when the degeneracy is lifted, as shown in Fig. 6(b).

The  $E_g$  doublet is special. As discussed in Sec. III, the complex orbital combinations do not carry angular momentum. The angular momentum operator  $L$ , projecting into this space, vanishes for all components. The  $\sigma_y$  term measure the octupole momentum  $\hat{f}_{xyz}$  instead, which is the lowest rank of non-vanishing multipole order for  $E_g$  orbitals. On the level of single-particle physics, the  $\sigma_y$  term cannot be obtained directly from the spin-orbit coupling in the  $E_g$  space. It can appear as a result of second-order perturbation, taking into account the virtual excitation from the  $E_g$  orbitals to the  $t_{2g}$  orbitals. As discussed in Eq. (3), the  $T_{2g}$  orbitals splits into one 1d irrep  $A_1$  and one 2d irrep  $E$  of the site symmetry group  $C_{3v}$ , which in general have distinct onsite energies. We denote the energy difference from the two irreps derived from the  $T_{2g}$  orbitals to the  $E_g$  orbitals as  $\Delta_1$  and  $\Delta_2$ , respectively. The second order spin-orbit coupling reads,

$$\begin{aligned} H'_\lambda &= -\lambda_0^2 P_{E_g} \left\{ \frac{\vec{L} \otimes \vec{S} P_{A_1} \vec{L} \otimes \vec{S}}{\Delta_1} + \frac{\vec{L} \otimes \vec{S} P_E \vec{L} \otimes \vec{S}}{\Delta_2} \right\} P_{E_g} \\ &= -\left( \frac{\lambda_0^2}{2\Delta_1} + \frac{\lambda_0^2}{\Delta_2} \right) \sigma_0 - \frac{\lambda_0^2}{\Delta_1 \Delta_2} (\Delta_1 - \Delta_2) \sigma_2 \otimes S_{(1,1,1)}, \end{aligned} \quad (44)$$

where  $P_{E_g}$ ,  $P_E$  and  $P_{A_1}$  are the projection operators, and  $S_{(1,1,1)}$  is the spin operator along the (1,1,1) direction. The first term is proportional to the identity operator

and thus can be absorbed into the chemical potential. The second represents the effective spin-orbit coupling in the  $E_g$  doublets with the spin-orbit coupling strength,

$$\lambda = \frac{\lambda_0^2}{\Delta_1 \Delta_2} (\Delta_1 - \Delta_2). \quad (45)$$

Recall that  $\Delta_1 - \Delta_2$  is the energy difference between the  $A_1$  and  $E$  irreps derived from the  $T_{2g}$  orbital in Eq. (3). Therefore, the energy splitting of the  $T_{2g}$  triplet under  $C_{3v}$  site symmetry is essential for nonzero  $\lambda$ .

The gaps introduced by the  $\sigma_y$  term in the orbital space are topological. It is straightforward to show that the four bands in Fig. 6(a) and (b) acquire Chern numbers 1, 0, 0, -1 from the bottom to the top. As a result, edge states appear on the boundary of the material. We consider the Hamiltonian on a ribbon with finite width but infinite length, in which case  $k_x$  remains a good quantum number. The spectrum is plotted in Fig. 7(a) as a function  $k_x$ , showing the edge states between the four bulk bands. The orbital wave functions of the edge states are in general complex. The expectation value of the  $\sigma_y$  operator in the orbital space is indicated by the color bar. When the orbital degree of freedom is the  $E_g$  doublet, the edge states carry the magnetic octupole moment instead of the dipole moment, sketched in Fig. 7(b).

The topological gaps are proportional to the coefficient  $\lambda$  of the  $\sigma_2$  term in the Hamiltonian. Remarkably, when the orbital degrees of freedom are realized by the  $(p_x, p_y)$ ,  $(d_{xz}, d_{yz})$  or  $(d_{xy}, d_{x^2-y^2})$ ,  $\lambda$  is directly related to the atomic spin-orbit coupling strength  $\lambda_0$ , which could be quite large for heavy atoms. This leads to a robust topological phase, such as quantum spin Hall effect, at high temperatures. In contrast, in  $E_g$  systems, the  $\sigma_2$  term comes from the second-order perturbation of the spin-orbit coupling. Therefore, in the  $E_g$  Dirac materials, the band degeneracy is much more stable than other realizations. Even though the quadratic band touching can be gaped out from dynamic spin-orbit coupling generated by interaction, the Dirac points are stable against interaction, making the  $E_g$  Dirac materials an ideal 2D Dirac semi-metal.

We also present the gap opening pattern from the staggering mass term  $H_m$  in Fig. 6(c), which is the same for different orbital realizations.  $H_m$  term leads to a trivial band insulator by itself. However, including  $H_m$  in the presence of  $H_\lambda$  can lead to richer topological phases with various Chern bands and edge state configurations [14].

## VII. THE INTERACTION EFFECTS

The interplay between the band structure and interaction can lead to many interesting phases of matter as a function of the filling fraction. In the following, we mention several most interesting ones.

At filling 1/2, the Fermi surface is at the Dirac points, which are stable against interaction. Therefore, the system remains a Dirac semi-metal for a while before it en-

ters a Mott insulator phase. In the Mott insulator, each site is occupied by two electrons. Because of the strong intra-orbital repulsion and Hund's coupling, the two electrons prefer to stay in two different orbitals and form a triplet. As a result, the low-energy effective theory of the Mott insulator is described by a spin 1 Heisenberg model on the honeycomb lattice where the orbital degrees of freedom are inert.

At filling 1/4, the bottom two spinful bands are filled. The Fermi surface is right at the quadratic band-touching point, which is unstable against interaction [43]. When the interaction is weak, it dynamically generates the spin-orbital coupling term in both  $p_x/p_y$  and  $E_g$  orbital-active Dirac material, which gives rise to the quantum spin Hall effect. As the interaction strength grows, the quantum spin Hall phase gives way to a nematic phase that breaks the 3-fold rotation symmetry.

At filling 1/8, the Fermi surface is within the bottom two spinful bands. In the strong anisotropy limit, the two bands become flat, which enhances the interaction effect. Due to the Coulomb interaction, the system favors a flat-band ferromagnetic state. Therefore, effectively, one of the spinful flat bands is filled, and the Fermi surface is at the quadratic band touching point again. The resulting weak interaction phase exhibits the anomalous quantum Hall effect.

As the filling becomes even lower due to the band flatness, the systems start to Wigner-crystallize. In particular, when the flat band is 1/3 filled, the localized states close-pack the lattice. If only on-site interactions are considered, such a close-packing many-body state is the *exact* many-body ground state with massive spin degeneracy from each localized single-particle state. This close-packing state breaks the original lattice translation symmetry with an enlarged  $\sqrt{3} \times \sqrt{3}$  unit cell, sketched in Fig. 4(b). When long-range interactions are considered, the Wigner crystal appears at even lower fillings. When the spin-orbit coupling is included, the flat band becomes nearly flat and acquires Chern number  $\pm 1$ . In this case, the Chern fractional insulator [42] also becomes a ground state candidate and competes with the Wigner crystal phase.

## VIII. DISCUSSION AND SUMMARY

We have studied the orbital-active Dirac materials in a unified manner. The various orbital realizations can be understood as the irreps of the point group symmetry  $C_{3v}$ . Both belonging to the two-dimensional  $E$  irrep of  $C_{3v}$ , the  $p_x/p_y$  doublet and the  $E_g$  doublet can map to each other, and the Dirac materials based on these two sets of different doublet has the same property. Based on the symmetry, we show the band structure features Dirac cones at  $K(K')$  points and a quadratic band touching  $\Gamma$ . The interplay between the interesting band structure and interaction leads to a rich phase diagram of the orbital-active Dirac materials.

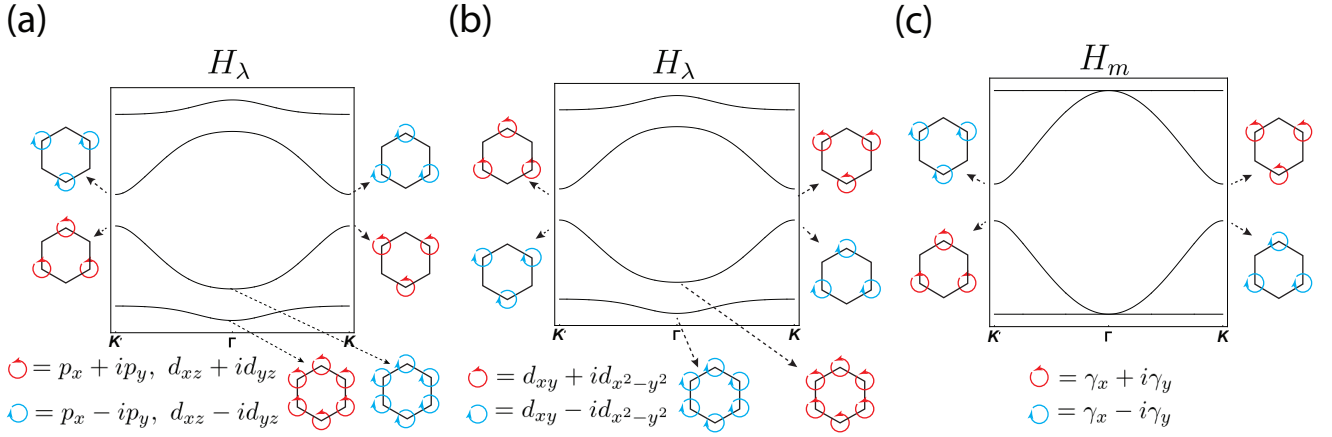


FIG. 6. (a) The gap opening pattern from the  $H_\lambda$  term for the  $(p_x, p_y)$  and  $(d_{xz}, d_{yz})$  doublets. (b) The gap opening pattern from the  $H_\lambda$  term for the  $(d_{xy}, d_{x^2-y^2})$  doublet. (c) The gap opening pattern from the stagger mass term for all cases. The complex orbital state naturally occurs at the  $K(K')$  point.

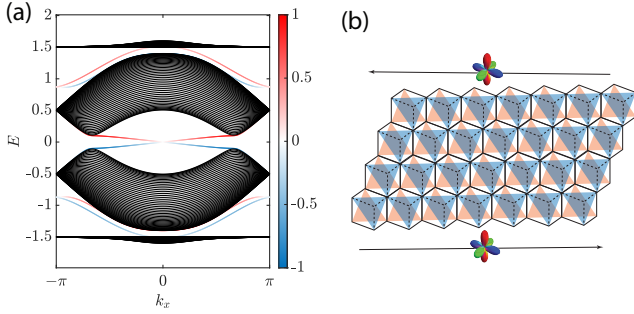


FIG. 7. (a) The spectrum of the Hamiltonian including  $H_\lambda$  term on a ribbon geometry.  $\lambda$  is set to  $0.2t_\parallel$ . Edge states appear between the bulk bands. The orbital wave function of the edges is complex, the chirality indicated by the color bar. (b) The ribbon geometry. When the orbital realization is from the  $E_g$  doublet, the edge states carry magnetic octupole momentum.

The Dirac material is not only limited to the electronic systems but also applies to systems of phonons and polaritons [30–35], where their polarization modes realize the orbital degrees of freedom. The symmetry argument in Sec. V also enforces chiral valley phonons in materials with a honeycomb structure, such as Boron Nitride and TMD. Thus the interplay between the chirality of electrons wave function and the chirality of the phonons opens a new door for valleytronics.

## IX. ACKNOWLEDGMENT

C. W. is supported by the National Natural Science Foundation of China through Grant No. 12174317, No. 11729402 and No. 12234016.

- 
- [1] M. Z. Hasan and C. L. Kane, Colloquium: Topological insulators, *Rev. Mod. Phys.* **82**, 3045 (2010).
  - [2] X. L. Qi and S. C. Zhang, Topological insulators and superconductors, *Rev. Mod. Phys.* **83**, 1057 (2011).
  - [3] N. P. Armitage, E. J. Mele, and A. Vishwanath, Weyl and Dirac semimetals in three-dimensional solids, *Rev. Mod. Phys.* **90**, 015001 (2018).
  - [4] A. H. C. Neto, F. Guinea, N. M. R. Peres, K. S. Novoselov, and A. K. Geim, The electronic properties of graphene, *Rev. Mod. Phys.* **81**, 109 (2007).
  - [5] S. Das Sarma, S. Adam, E. H. Hwang, and E. Rossi, Electronic transport in two-dimensional graphene, *Rev. Mod. Phys.* **83**, 407 (2011).
  - [6] C. Wu, D. Bergman, L. Balents, and S. Das Sarma, Flat bands and wigner crystallization in the honeycomb optical lattice, *Phys. Rev. Lett.* **99**, 070401 (2007).
  - [7] C. Wu and S. Das Sarma,  $p_{x,y}$ -orbital counterpart of graphene: Cold atoms in the honeycomb optical lattice, *Phys. Rev. B* **77**, 235107 (2008).
  - [8] D. Xiao, W. Zhu, Y. Ran, N. Nagaosa, and S. Okamoto, Interface engineering of quantum Hall effects in digital transition metal oxide heterostructures, *Nat. Commun.* **2**, 596 (2011).
  - [9] A. Rüegg and G. A. Fiete, Topological insulators from complex orbital order in transition-metal oxides heterostructures, *Phys. Rev. B* **84**, 201103 (2011).
  - [10] K.-Y. Yang, W. Zhu, D. Xiao, S. Okamoto, Z. Wang, and Y. Ran, Possible interaction driven topological phases in (111) bilayers of  $\text{LaNiO}_3$ , *Phys. Rev. B* **84**, 201104 (2011).
  - [11] X. Qian, J. Liu, L. Fu, and J. Li, Quantum Spin Hall Effect and Topological Field Effect Transistor in Two - Dimensional T ransition Metal Dichalcogenides, *Science* (80-. ). **346**, 1344 (2014).
  - [12] Y. Xu, B. Yan, H. J. Zhang, J. Wang, G. Xu, P. Tang, W. Duan, and S. C. Zhang, Large-gap quantum spin

- hall insulators in tin films, *Phys. Rev. Lett.* **111**, 136804 (2013).
- [13] S.-C. Wu, G. Shan, and B. Yan, Prediction of Near-Room-Temperature Quantum Anomalous Hall Effect on Honeycomb Materials, *Phys. Rev. Lett.* **113**, 256401 (2014).
- [14] G.-F. Zhang, Y. Li, and C. Wu, Honeycomb lattice with multiorbital structure: Topological and quantum anomalous Hall insulators with large gaps, *Phys. Rev. B* **90**, 075114 (2014).
- [15] F. Reis, G. Li, L. Dudy, M. Bauernfeind, S. Glass, W. Hanke, R. Thomale, J. Schäfer, and R. Claessen, Bismuthene on a SiC substrate: A candidate for a high-temperature quantum spin Hall material, *Science* (80-. ). **357**, 287 (2017).
- [16] Y. Xia, S. Jin, W. Hanke, R. Claessen, and G. Li, High-temperature quantum spin hall states in buckled iii-v-monolayer/sio<sub>2</sub>, *arXiv preprint arXiv:2112.13483* (2021).
- [17] S. Jin, Y. Xia, W. Shi, J. Hu, R. Claessen, W. Hanke, R. Thomale, and G. Li, Large-gap quantum anomalous hall states induced by functionalizing buckled bi-iii monolayer/al 2 o 3, *Physical Review B* **106**, 125151 (2022).
- [18] Z. F. Wang, Z. Liu, and F. Liu, Organic topological insulators in organometallic lattices, *Nat. Commun.* **4**, 1471 (2013).
- [19] Z. F. Wang, Z. Liu, and F. Liu, Quantum Anomalous Hall Effect in 2D Organic Topological Insulators, *Phys. Rev. Lett.* **110**, 196801 (2013).
- [20] G. Chen, L. Jiang, S. Wu, B. Lyu, H. Li, B. L. Chittari, K. Watanabe, T. Taniguchi, Z. Shi, J. Jung, Y. Zhang, and F. Wang, Evidence of a gate-tunable Mott insulator in a trilayer graphene moiré superlattice, *Nat. Phys.* **15**, 237 (2019).
- [21] Y. Cao, V. Fatemi, S. Fang, K. Watanabe, T. Taniguchi, E. Kaxiras, and P. Jarillo-Herrero, Unconventional superconductivity in magic-angle graphene superlattices, *Nature* **556**, 43 (2018).
- [22] Y. Cao, V. Fatemi, A. Demir, S. Fang, S. L. Tomarken, J. Y. Luo, J. D. Sanchez-Yamagishi, K. Watanabe, T. Taniguchi, E. Kaxiras, *et al.*, Correlated insulator behaviour at half-filling in magic-angle graphene superlattices, *Nature* **556**, 80 (2018).
- [23] M. Yankowitz, S. Chen, H. Polshyn, Y. Zhang, K. Watanabe, T. Taniguchi, D. Graf, A. F. Young, and C. R. Dean, Tuning superconductivity in twisted bilayer graphene, *Science* **363**, 1059 (2019).
- [24] H. C. Po, L. Zou, A. Vishwanath, and T. Senthil, Origin of Mott Insulating Behavior and Superconductivity in Twisted Bilayer Graphene, *Phys. Rev. X* **8**, 031089 (2018).
- [25] N. F. Q. Yuan and L. Fu, Model for the metal-insulator transition in graphene superlattices and beyond, *Phys. Rev. B* **98**, 045103 (2018).
- [26] C.-C. Liu, L.-D. Zhang, W.-Q. Chen, and F. Yang, Chiral spin density wave and  $d + id$  superconductivity in the magic-angle-twisted bilayer graphene, *Phys. Rev. Lett.* **121**, 217001 (2018).
- [27] J. W. F. Venderbos and R. M. Fernandes, Correlations and electronic order in a two-orbital honeycomb lattice model for twisted bilayer graphene, *Physical Review B* **98**, 245103 (2018).
- [28] J. F. Dodaro, S. A. Kivelson, Y. Schattner, X. Q. Sun, and C. Wang, Phases of a phenomenological model of twisted bilayer graphene, *Physical Review B* **98**, 075154 (2018).
- [29] M. Fidrysiak, M. Zegrodnik, and J. Spałek, Unconventional topological superconductivity and phase diagram for an effective two-orbital model as applied to twisted bilayer graphene, *Physical Review B* **98**, 085436 (2018).
- [30] T. Jacqmin, I. Carusotto, I. Sagnes, M. Abbarchi, D. D. Solnyshkov, G. Malpuech, E. Galopin, A. Lemaître, J. Bloch, and A. Amo, Direct Observation of Dirac Cones and a Flatband in a Honeycomb Lattice for Polaritons, *Phys. Rev. Lett.* **112**, 116402 (2014).
- [31] M. Milićević, T. Ozawa, G. Montambaux, I. Carusotto, E. Galopin, A. Lemaître, L. Le Gratiet, I. Sagnes, J. Bloch, and A. Amo, Orbital Edge States in a Photonic Honeycomb Lattice, *Phys. Rev. Lett.* **118**, 10.1103/PhysRevLett.118.107403 (2017).
- [32] L. Zhang and Q. Niu, Chiral Phonons at High-Symmetry Points in Monolayer Hexagonal Lattices, *Phys. Rev. Lett.* **115**, 115502 (2015).
- [33] S. Roman and D. H. Sebastian, Observation of phononic helical edge states in a mechanical topological insulator, *Science* (80-. ). **349**, 47 (2015).
- [34] O. Stenull, C. L. Kane, and T. C. Lubensky, Topological Phonons and Weyl Lines in Three Dimensions, *Phys. Rev. Lett.* **117**, 068001 (2016).
- [35] H. Zhu, J. Yi, M. Y. Li, J. Xiao, L. Zhang, C. W. Yang, R. A. Kaindl, L. J. Li, Y. Wang, and X. Zhang, Observation of chiral phonons, *Science* (80-. ). **359**, 579 (2018).
- [36] P. Santini and G. Amoretti, Magnetic-Octupole Order in Neptunium Dioxide?, *Phys. Rev. Lett.* **85**, 2188 (2000).
- [37] J. van den Brink and D. Khomskii, Orbital ordering of complex orbitals in doped Mott insulators, *Phys. Rev. B* **63**, 140416 (2001).
- [38] Y. Kuramoto, H. Kusunose, and A. Kiss, Multipole Orders and Fluctuations in Strongly Correlated Electron Systems, *J. Phys. Soc. Japan* **78**, 072001 (2009).
- [39] G. Jackeli and G. Khaliullin, Magnetically hidden order of kramers doublets in  $d^1$  systems: Sr<sub>2</sub>VO<sub>4</sub>, *Phys. Rev. Lett.* **103**, 067205 (2009).
- [40] Y.-D. Li, X. Wang, and G. Chen, Hidden multipolar orders of dipole-octupole doublets on a triangular lattice, *Phys. Rev. B* **94**, 201114 (2016).
- [41] J.-W. Rhim, K. Kim, and B.-J. Yang, Quantum distance and anomalous landau levels of flat bands, *Nature* **584**, 59 (2020).
- [42] K. Sun, Z. Gu, H. Katsura, and S. Das Sarma, Nearly flatbands with nontrivial topology, *Phys. Rev. Lett.* **106**, 236803 (2011).
- [43] K. Sun, H. Yao, E. Fradkin, and S. A. Kivelson, Topological insulators and nematic phases from spontaneous symmetry breaking in 2D fermi systems with a quadratic band crossing, *Phys. Rev. Lett.* **103**, 046811 (2009).

### Appendix A: The $C_{3v}$ group and its double group $C_{3v}^D$

The  $C_{3v}$  point group is the simplest non-abelian group, containing six elements generating by a three-fold rotation and an in-plane reflection. It has three irreps  $A_1$ ,  $A_2$  and  $E$ . The first two are one-dimensional while the last one is two-dimensional. The  $A_1$  irrep is trivial and examples include  $s$  orbitals and  $p_z$  orbitals; the  $A_2$  irrep is odd under the reflection with realizations such as pseudovector  $L_z$  and  $f$  orbital  $y(3x^2 - y^2)$ . In this work, we are mostly interested in the two-dimensional  $E$  irrep.

The  $C_{3v}$  group includes 6 operations in 3 conjugacy classes: the identity  $I$ , the 3-fold rotations  $\{C_3^1, C_3^2\}$  around the vertical axis, and the reflection operations with respect to three vertical planes  $\{\sigma_{v_i}\}$  with  $i = 1 \sim 3$ . It possesses two one-dimensional representations  $A_1$  and  $A_2$ , and one two-dimensional representation  $E$ . Their character table is presented in Tab A. The bases of the  $A_{1,2}$  representations carry angular momentum quantum number  $L_z = 0$ , and those of the  $E$  representation can be chosen with  $L_z = \pm 1$ .

	$I$	$2C_3$	$3\sigma_v$
$A_1$	1	1	1
$A_2$	1	1	-1
$E$	2	-1	0

TABLE I. The character table of the  $C_{3v}$  group, which has two one dimensional representations  $A_{1,2}$  and one two-dimensional representation  $E$ .  $A_{1,2}$  carry orbital angular momentum  $L_z = 0$ , and  $E$  carries  $L_z = \pm 1$ .

In the presence of spin-orbit coupling,  $C_{3v}$  is augmented to its double group  $C_{3v}^D = C_{3v} + \bar{C}_{3v}$ .  $\bar{C}_{3v} = \bar{I}C_{3v}$  is the coset by multiplying  $\bar{I}$  to  $C_{3v}$ , where  $\bar{I}$  is the rotation of  $2\pi$ . The  $C_{3v}^D$  group has six conjugacy classes, and hence six non-equivalent irreducible representations whose characteristic table is presented in Tab. A.  $A_{1,2}$  and  $E$  remain the representations of  $C_{3v}^D$  of integer angular momentum, for which  $\bar{I}$  is the same as the identity operation. In addition,  $C_{3v}^D$  also possesses half-integer angular momentum representations, for which  $\bar{I}$  is represented as the negative of the identity matrix. For example, a new two-dimensional representation  $E_{\frac{1}{2}}$  appears corresponding to the angular momentum  $J_z = \pm \frac{1}{2}$ . The cases of  $J_z = \pm \frac{3}{2}$  are often denoted as the  $E_{\frac{3}{2}}$  representation. Actually, they are not an irreducible two-dimensional representation, but two non-equivalent one-dimensional representations. The two bases of  $\psi_{J_z=\pm\frac{3}{2}}$  are equivalent under the 3-fold rotations since  $\frac{3}{2} \equiv -\frac{3}{2} \pmod{3}$ , and neither of them are eigenstates of the reflections  $\sigma_v$  and  $\bar{\sigma}_v = \bar{I}\sigma_v$ . Instead, their superpositions  $\frac{1}{\sqrt{2}}(\psi_{\frac{3}{2}} \pm i\psi_{-\frac{3}{2}})$  carry the characters of  $\pm i$  for  $\sigma_v$  and  $\mp i$  for  $\bar{\sigma}_v$ , respectively.

	$I$	$\bar{I}$	$\{C_3^1, \bar{C}_3^2\}$	$\{C_3^2, \bar{C}_3^1\}$	$3\sigma_v$	$3\bar{\sigma}_v$
$E_{\frac{1}{2}}$	2	-2	1	-1	0	0
$E_{\frac{3}{2}}$	1	-1	-1	1	$i$	$-i$
	1	-1	-1	1	$-i$	$i$

TABLE II. Spinor representations for the  $C_{3v}^D$  group: The two-dimensional representation  $E_{\frac{1}{2}}$  is of  $J_z = \pm \frac{1}{2}$ .  $E_{\frac{3}{2}}$  splits into two non-equivalent one-dimensional representations with different characters under vertical reflections.

### Appendix B: Spherical tensor operators in the $d$ -orbital space

In the Hilbert space of  $d$  orbitals, the angular momentum operators are defined in the standard way

$$\hat{L}_x = \begin{pmatrix} 0 & 1 & 0 & 0 & 0 \\ 1 & 0 & \sqrt{\frac{3}{2}} & 0 & 0 \\ 0 & \sqrt{\frac{3}{2}} & 0 & \sqrt{\frac{3}{2}} & 0 \\ 0 & 0 & \sqrt{\frac{3}{2}} & 0 & 1 \\ 0 & 0 & 0 & 1 & 0 \end{pmatrix}, \quad \hat{L}_y = \begin{pmatrix} 0 & -i & 0 & 0 & 0 \\ i & 0 & -i\sqrt{\frac{3}{2}} & 0 & 0 \\ 0 & i\sqrt{\frac{3}{2}} & 0 & -i\sqrt{\frac{3}{2}} & 0 \\ 0 & 0 & i\sqrt{\frac{3}{2}} & 0 & -i \\ 0 & 0 & 0 & i & 0 \end{pmatrix}, \quad \hat{L}_z = \begin{pmatrix} 2 & 0 & 0 & 0 & 0 \\ 0 & 1 & 0 & 0 & 0 \\ 0 & 0 & 0 & 0 & 0 \\ 0 & 0 & 0 & -1 & 0 \\ 0 & 0 & 0 & 0 & -2 \end{pmatrix} \quad (\text{B1})$$



The total angular momentum operator  $\hat{L}^2 = \hat{L}_x^2 + \hat{L}_y^2 + \hat{L}_z^2$ , and the ladder operators  $\hat{L}_\pm = \hat{L}_x \pm \hat{L}_y$ . The spherical tensors  $\hat{Y}_{lm}$  satisfy the following commutation relation,

$$[L_+, Y_{l,m}] = \sqrt{(l-m)(l+m+1)} Y_{l,m+1} \quad (\text{B2})$$

Fixing  $l$ , the tensor operator with the lowest  $m$  can be easily expressed as powers of  $\hat{L}_-$ ,

$$\hat{Y}_{l,-l} = \frac{\sqrt{(2l)!}}{2^l l!} (\hat{L}_-)^l \quad (\text{B3})$$

Based on these relations, the general rank  $l$  spherical tensors can be constructed systematically from the angular momentum operators. All 25 linear independent operators acting on  $d$  orbitals can be organized into spherical tensor operators with rank  $0 \sim 4$ . The rank 1 tensor operators are,

$$\hat{Y}_{1,-1} = \frac{1}{\sqrt{2}} \hat{L}_-, \quad \hat{Y}_{1,0} = \hat{L}_z, \quad \hat{Y}_{1,1} = -\frac{1}{\sqrt{2}} \hat{L}_+ \quad (\text{B4})$$

The rank 2 tensor operators are

$$\hat{Y}_{2,-2} = \sqrt{\frac{3}{8}} \hat{L}_-^2, \quad \hat{Y}_{2,-1} = \sqrt{\frac{3}{2}} \overline{\hat{L}_- \hat{L}_z}, \quad \hat{Y}_{2,0} = \frac{1}{2} (2\hat{L}_z^2 - \hat{L}_x^2 - \hat{L}_y^2), \quad \hat{Y}_{2,1} = -\sqrt{\frac{3}{2}} \overline{\hat{L}_+ \hat{L}_z}, \quad \hat{Y}_{2,2} = \sqrt{\frac{3}{8}} \hat{L}_+^2 \quad (\text{B5})$$

where bars over the operators represent the average over all possible operators ordering. The rank three tensor operators are

$$\begin{aligned} \hat{Y}_{3,-3} &= \frac{\sqrt{5}}{4} \hat{L}_-^3, \quad \hat{Y}_{3,-2} = \sqrt{\frac{15}{8}} \overline{\hat{L}_-^2 \hat{L}_z}, \quad \hat{Y}_{3,-1} = \frac{\sqrt{3}}{4} \overline{\hat{L}_- (4\hat{L}_z^2 - \hat{L}_x^2 - \hat{L}_y^2)}, \quad \hat{Y}_{3,0} = \frac{1}{2} \overline{\hat{L}_z (2\hat{L}_z^2 - 3\hat{L}_x^2 - 3\hat{L}_y^2)} \\ \hat{Y}_{3,1} &= -\frac{\sqrt{3}}{4} \overline{\hat{L}_+ (4\hat{L}_z^2 - \hat{L}_x^2 - \hat{L}_y^2)}, \quad \hat{Y}_{3,2} = \sqrt{\frac{15}{8}} \overline{\hat{L}_+^2 \hat{L}_z}, \quad \hat{Y}_{3,3} = -\frac{\sqrt{5}}{4} \hat{L}_+^3. \end{aligned} \quad (\text{B6})$$

Lastly, the rank 4 tensors are

$$\begin{aligned} \hat{Y}_{4,-4} &= \sqrt{\frac{35}{128}} \hat{L}_-^4, \quad \hat{Y}_{4,-3} = \frac{\sqrt{35}}{4} \overline{\hat{L}_-^3 \hat{L}_z}, \quad \hat{Y}_{4,-2} = \sqrt{\frac{5}{32}} \overline{\hat{L}_-^2 (7\hat{L}_z^2 - \hat{L}^2)}, \quad \hat{Y}_{4,-1} = \frac{\sqrt{5}}{4} \overline{\hat{L}_- \hat{L}_z (7\hat{L}_z^2 - 3\hat{L}^2)} \\ \hat{Y}_{4,0} &= \frac{1}{8} \overline{(35\hat{L}_z^4 - 30\hat{L}_z^2 \hat{L}^2 + 3\hat{L}^4)}, \quad \hat{Y}_{4,1} = -\frac{\sqrt{5}}{4} \overline{\hat{L}_+ \hat{L}_z (7\hat{L}_z^2 - 3\hat{L}^2)}, \quad \hat{Y}_{4,2} = \sqrt{\frac{5}{32}} \overline{\hat{L}_+^2 (7\hat{L}_z^2 - \hat{L}^2)} \\ \hat{Y}_{4,3} &= -\frac{\sqrt{35}}{4} \overline{\hat{L}_+^3 \hat{L}_z}, \quad \hat{Y}_{4,4} = \sqrt{\frac{35}{128}} \hat{L}_+^4. \end{aligned} \quad (\text{B7})$$